RSC Advances

PAPER

View Article Online
View Journal | View Issue

Cite this: *RSC Adv.*, 2025, **15**, 46391

One-step sprayable durable superhydrophobic coatings based on discrete epoxy binders: fabrication and performance

Xuejuan Liu, [abc] Xin Liu,[d] Xinru Zhang[a] and Lei Wang*[e]

Superhydrophobic coatings demonstrate considerable application potential across diverse fields, including architecture, transportation, energy, and marine engineering. Among various preparation techniques, the one-step spraying method has emerged as a highly attractive strategy for fabricating superhydrophobic coatings owing to its significant advantages for large-scale production and operational simplicity. However, the superhydrophobic coatings currently prepared *via* the one-step spraying typically suffer from critical limitations of inadequate mechanical robustness and poor environmental durability, which severely constrain their practical deployment. This study innovatively proposes and employs a discrete epoxy resin adhesive system, aiming to effectively address the durability challenges inherent to one-step sprayed superhydrophobic coatings. Research findings demonstrate that the coatings fabricated using this approach retain exceptional superhydrophobicity (contact angle >150°, rolling angle <10°) even after rigorous testing regimes, including sandpaper abrasion, tape peeling, chemical corrosion, and ultraviolet (UV) aging. Consequently, their durability is significantly enhanced. This work provides an effective solution for developing high-performance superhydrophobic coatings that simultaneously feature a straightforward preparation process (one-step spraying) and excellent durability. It thereby holds significant value for advancing the large-scale practical application of this technology.

Received 14th September 2025
Accepted 12th November 2025

DOI: 10.1039/d5ra06946g

rsc.li/rsc-advances

1. Introduction

The design of superhydrophobic coatings draws inspiration from the unique hydrophobic phenomenon observed in nature, exemplified by the "lotus effect" exhibited by lotus leaves.[1] The fundamental approach to achieving superhydrophobicity lies in the synergistic construction of micro-nano-scale surface roughness with the modification of low-surface-energy chemical substances.[2–4] This combination endows the surface with extreme water repellency, typically characterized by an apparent water contact angle (WCA) exceeding 150° and a rolling angle (RA) below 10°.[5–7] This superhydrophobic behavior originates from the Cassie–Baxter wetting state established when water droplets interact with the micro-nano rough structures.[8] Within this state, the actual contact area between the water droplet and the solid surface is substantially reduced, resulting in a dramatic decrease in solid–liquid interfacial adhesion.[9] It is this minimal interfacial adhesion that confers unique properties upon superhydrophobic surfaces, including self-cleaning capability, as well as anti-icing, anti-corrosion, and drag-reduction characteristics.[10] Consequently, these surfaces exhibit significant application potential across diverse fields such as architectural glass curtain walls, solar panels, marine antifouling, transmission line de-icing, and microfluidic devices.[11,12]

The current fabrication strategies for the superhydrophobic coatings primarily include template-based methods, etching techniques, sol–gel processes, chemical vapor deposition (CVD), and spraying methods.[13–16] Among these, the one-step spraying method is considered one of the most promising technical routes for industrialization owing to its significant process advantages.[17] The core principle of this method involves simultaneously dispersing polymer binders (*e.g.*, resins) and nanoparticles modified with low-surface-energy substances (*e.g.*, silanes or fluorinated compounds) in a suitable solvent to form a uniform and stable dispersion system. This dispersion is subsequently sprayed directly onto the target substrate surface. During the subsequent drying/curing stage, the nanoparticles self-assemble to construct micro-nano-scale rough surface structures, while the polymer binders cross-link and cure, achieving robust bonding between the nanostructured layer and the substrate. Ultimately, this process forms

[a]*College of Life Science, Langfang Normal University, Langfang 065000, Hebei, China*
[b]*Technical Innovation Center for Utilization of Edible and Medicinal Fungi in Hebei Province, Langfang 065000, Hebei, China*
[c]*Langfang Key Laboratory for Biological Sample Analysis and Pesticide Residue Detection, Langfang Normal University, Langfang 065000, Hebei, China*
[d]*Hebei Chengzhu Zhiyan New Materials Technology Co., Ltd, Baoding 071000, Hebei, China*
[e]*State Key Laboratory of Efficient Production of Forest Resources, Beijing Key Laboratory of Lignocellulosic Chemistry, Beijing Forestry University, Beijing 100083, China. E-mail: leiwangns@bjfu.edu.cn*

a superhydrophobic surface.[18] The paramount advantage of this technique is its single-step fabrication characteristic – the functional coating can be deposited in a single spraying operation, eliminating the need for additional post-treatment procedures. This feature confers operational simplicity, low equipment demands, substrate shape independence, and excellent potential for large-area preparation and scalable manufacturing.[19,20]

Numerous studies have utilized the one-step spraying method to fabricate superhydrophobic coatings. For instance, Su *et al.*[21] dispersed polytetrafluoroethylene (PTFE) particles and fluorinated epoxy resin in a butyl-acetate solvent. Spraying this dispersion yielded a superhydrophobic surface exhibiting a WCA of 160° ± 0.4° and a RA of approximately 5°. However, this coating lost its superhydrophobicity after only 4.4 m of linear abrasion under a 400-grit sandpaper with a 100 g load. Similarly, Zhao *et al.*[22] reported a coating prepared by blending and spraying fluorinated silica nanoparticles with epoxy resin, achieving a WCA of 162° and a RA of 2.3°. Nevertheless, it failed after 5.5 m of abrasion under a 360-grit sandpaper with a 200 g load. The research by Wang *et al.*[23] further demonstrated that a sprayed coating based on an epoxy resin/silica nanoparticle system sustained an abrasion distance of merely 4 m under conditions employing 1000-grit sandpaper and a 50 g load. Pakzad *et al.*[24] attempted to enhance durability by incorporating a small amount of polydimethylsiloxane (PDMS) into an epoxy resin/hydrophobic nanoparticle system. The resulting coating displayed a WCA of 154.6°, yet its abrasion resistance was limited to 3.75 m under an 800-grit sandpaper with a 100 g load. Collectively, these studies consistently demonstrate that while the one-step spraying method offers process simplicity, the resultant superhydrophobic coatings typically exhibit critically insufficient mechanical durability. The primary failure mechanism is attributed to solvent evaporation kinetics during droplet drying: the preferential evaporation of the solvent on the surface induces outward Marangoni or capillary flows. These flows continuously transport and enrich nanoparticles towards the gas–liquid interface. Consequently, upon drying, the coating surface forms a micro-nano rough structure rich in nanoparticles, while the underlying layer solidifies into a dense, smooth polymer binder matrix largely devoid of particles. Therefore, when mechanical stress destroys the inherently wear-prone surface roughness, the exposed smooth underlying layer lacks both the requisite micro-nano topography and low surface energy characteristics, leading to the immediate loss of the coating's overall superhydrophobicity.[25–27]

Recently, utilizing binder phase separation to construct self-similar structures has emerged as a highly effective strategy for enhancing the mechanical durability of the one-step sprayed superhydrophobic coatings. For instance, pioneering studies by Wei *et al.* have demonstrated robust superamphiphobic coatings using flexible or thermoplastic binders like silicone-modified polyester and polyolefin.[28,29] These works brilliantly showcase the universality and potential of this approach. However, the feasibility and mechanism of employing a rigid, high-strength binder system, such as epoxy resin, *via* a similar phase-separation pathway remain an open question.

To fundamentally address this bottleneck, we propose a strategy based on a phase-separated, discrete epoxy binder system. The core design principle involves precipitating a conventional epoxy resin (dissolved in a good solvent like butyl acetate) into discrete micro-aggregates using a poor solvent (absolute ethanol). This process is governed by a decrease in the solvent quality, which reduces the solubility of the polymer chains, triggering the nucleation and growth of resin-rich domains. These discrete aggregates, when blended with low-surface-energy nanoparticles (SiO_2@PFDTES), co-assemble during the spray deposition and solvent evaporation phase. Unlike conventional systems where nanoparticles are swept to the surface, this co-assembly synergistically constructs a gradient, porous micro-nano structure that extends throughout the coating's thickness. Consequently, even upon the abrasion-induced removal of the surface layer, the newly exposed subsurface retains sufficient nanoparticles and micro-nano roughness to maintain superhydrophobicity, a mechanism we term 'structural regeneration'. This approach seeks to fundamentally enhance the coating's mechanical robustness and long-term environmental durability through rational structural design.

2. Experiment

2.1 Experimental reagents and materials

The solvents employed in this study were butyl acetate (purity ≥99.5%) and absolute ethanol (purity ≥99.5%), both procured from Energy Chemical. Epoxy resin (E44) and its curing agent, polyetheramine D230, were obtained from Nantong Star Synthetic Material Co., Ltd (Shanghai, China). Fumed silica nanoparticles (approximate particle size: 20 nm) were supplied by Hubei Huifu Nano Materials Co., Ltd (Yichang, China). The nanoparticle surface modification was conducted using the following reagents: 1H,1H,2H,2H-perfluorodecyltriethoxysilane (PFDTES, purity ≥97%), ammonia water (analytical grade), and tetraethyl orthosilicate (TEOS, purity ≥98%), all sourced from Shanghai Macklin Chemical Technology Co., Ltd. Tinned iron sheets (dimensions: 120 mm × 70 mm) served as the substrate material. Prior to the coating deposition, the substrate surfaces underwent ultrasonic cleaning in butyl acetate for 10 min and were subsequently dried.

2.2 Method for preparing fluorosilane-modified silica nanoparticles

Initially, 20 g of silica nanoparticles was dispersed in 1 L of an ethanol/ammonia solution (volume ratio: 23 : 2). The mixture was subjected to ultrasonic treatment for 30 min to ensure sufficient dispersion. Subsequently, 3 mL of PFDTES and 3 mL of TEOS were added sequentially. The reaction proceeded under vigorous magnetic stirring at room temperature for 2 h. The resulting product was isolated by centrifugation and washed three times with butyl acetate to remove the unreacted species. Finally, the modified nanoparticles were dried in a vacuum oven at 60 °C for 12 h, yielding fluorosilane-modified silica nanoparticles (SiO_2@PFDTES).

The chemical composition of the synthesized SiO_2@PFDTES nanoparticles was characterized by Fourier Transform Infrared Spectroscopy (FTIR, Nicolet iS50) in the range of 4000–400 cm^{-1}. The surface elemental composition and distribution were analyzed using a field-emission scanning electron microscope (FE-SEM, ZEISS) equipped with an Energy Dispersive X-ray Spectroscopy (EDS) detector.

2.3 Coating preparation method

Initially, 4.0 g of epoxy resin (E44) was dissolved in 3.0 g of butyl acetate. Under magnetic stirring at 600 rpm, 25.0 g of absolute ethanol was introduced dropwise to induce the phase separation of the epoxy resin, resulting in the formation of micro-aggregates. After maintaining stirring for 30 min, 4.0 g of the SiO_2@PFDTES nanoparticles was incorporated. Stirring was maintained for an additional 2 h to ensure uniform dispersion. Subsequently, 1.33 g of a curing agent, D230, was added. Following 10 min of stirring, a stable dispersion suitable for superhydrophobic coating application was obtained. This dispersion was then applied onto the substrate *via* a spray gun, with parameters set to a compressed air pressure of 0.5 MPa, a spray distance of 15–20 cm, and directed perpendicularly to the substrate surface. The sprayed substrate was transferred to a forced-air oven and cured at 80 °C for 2 h, yielding the final superhydrophobic coating.

2.4 Coating performance characterization

2.4.1 Surface wettability characterization. The WCA and RA were measured using a contact angle goniometer (DSA 255, Krüss GmbH, Germany) with 5 μL deionized water droplets under ambient conditions. The reported values represent the average of measurements taken at 5 distinct locations on each sample surface.

2.4.2 Surface morphology analysis. The surface morphology of the coatings was characterized using field-emission scanning electron microscopy (FE-SEM, ZEISS).

2.4.3 Abrasion resistance testing. The coated samples were inverted onto a 1000-grit sandpaper under a normal pressure of 1.1 kPa. The samples were translated linearly for a distance of 10 cm in one direction and then returned for a distance of 10 cm to the starting position; this sequence constituted one abrasion cycle. The WCA and RA were measured after every 5 cycles. The abrasion resistance was quantified as the cumulative linear abrasion distance (meters) at which the coating failed to maintain superhydrophobicity (defined as WCA < 150° or RA > 10°).

2.4.4 Coating adhesion testing (tape peel). Clean, dry coated samples were subjected to adhesion testing. A 25 mm wide strip of a 3 M adhesive tape was firmly applied to the coating surface. A 500 g cylindrical weight was rolled unidirectionally over the tape surface several times to ensure intimate contact and eliminate air bubbles. After allowing the tape to adhere for 2 min, it was peeled from the surface at a constant speed of 50 mm min^{-1} with a peel angle of 120°. The WCA and RA were recorded after a single peel cycle. Adhesion strength was assessed by the number of consecutive peel cycles required to induce the loss of superhydrophobicity.

2.4.5 Chemical corrosion resistance. The coated samples were fully immersed in aqueous solutions of HCl (pH = 2), NaOH (pH = 12), and NaCl (3.5 wt%) at ambient temperature. After 10 days of immersion, the samples were removed, rinsed with deionized water, and dried, and the WCA and RA were measured to evaluate the chemical resistance.

2.4.6 UV aging resistance. The samples were exposed to continuous UV irradiation in a chamber (wavelength: 365 nm, intensity: 5800 mW cm^{-2}) at a constant temperature of 25 ± 1 °C. The WCA and RA were monitored hourly to quantify the UV degradation resistance.

2.4.7 Thermal cycling stability. The samples underwent thermal cycling by holding at −20 °C for 20 min and then at 150 °C for 20 min, and subsequently cooling to room temperature (25 °C) *via* natural convection. The WCA and RA were measured immediately after the completion of each full thermal cycle to assess the impact of the alternating thermal stress on the hydrophobicity.

2.4.8 Long-term anti-wettability (water immersion). The samples were submerged in deionized water maintained at 25 °C. The WCA and RA were measured every 24 h over a period of 7 days to evaluate the coating's resistance to prolonged water exposure.

2.5 Statistical analysis

All quantitative experiments in this study, including contact angle, sliding angle, and durability tests, were repeated at least five times ($n \geq 5$) on independently prepared samples to ensure reproducibility. The data are presented throughout the manuscript as the mean value plus or minus the standard deviation (mean ± SD). To determine the statistical significance of the differences observed between groups, a one-way analysis of variance (ANOVA) was performed, followed by Tukey's post-hoc test for multiple comparisons. A probability value of $p < 0.05$ was considered statistically significant. All statistical analyses were performed using OriginPro 2022.

3. Results and discussion

3.1 SiO_2@PFDTES nanoparticles and morphological characterization

The successful modification of the silica nanoparticles with PFDTES was first confirmed by FTIR. As shown in Fig. 1a, the spectrum of the SiO_2@PFDTES nanoparticles exhibits distinct absorption bands at approximately 1207 cm^{-1} and 1151 cm^{-1}, which are attributed to the stretching vibrations of C–F bonds. These characteristic peaks, which are absent in the spectrum of pristine SiO_2, provide evidence for the successful introduction of low-surface-energy fluorocarbon chains onto the nanoparticle surface. Further evidence was obtained from EDS analysis. The elemental mapping images shown in Fig. 1b and c reveal a uniform and dense distribution of the fluorine (F) element across the SiO_2@PFDTES agglomerates, confirming the homogeneity of the modification. This uniform fluorination is

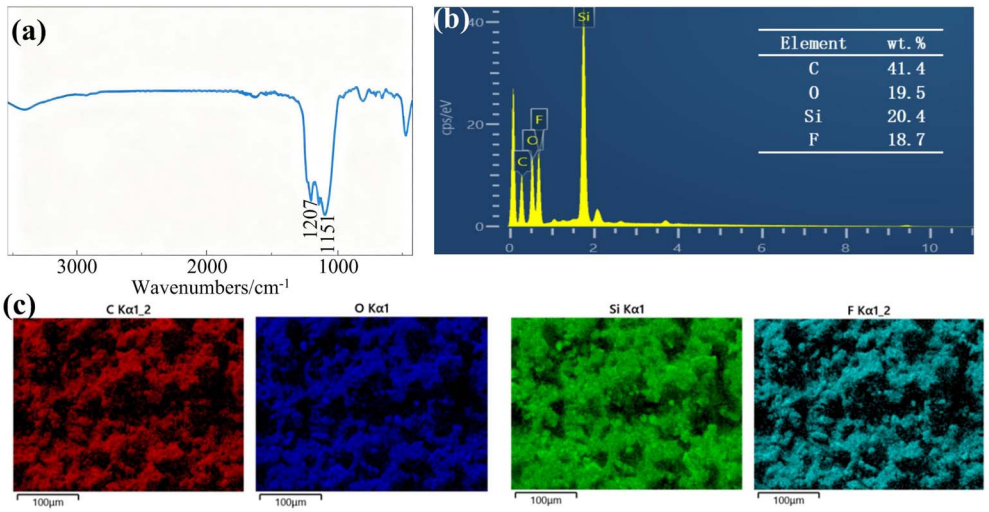

Fig. 1 Characterization of the SiO_2@PFDTES nanoparticles. (a) FTIR spectra of the SiO_2@PFDTES nanoparticles. (b) EDS spectrum and (c) elemental distribution maps of the superhydrophobic coating.

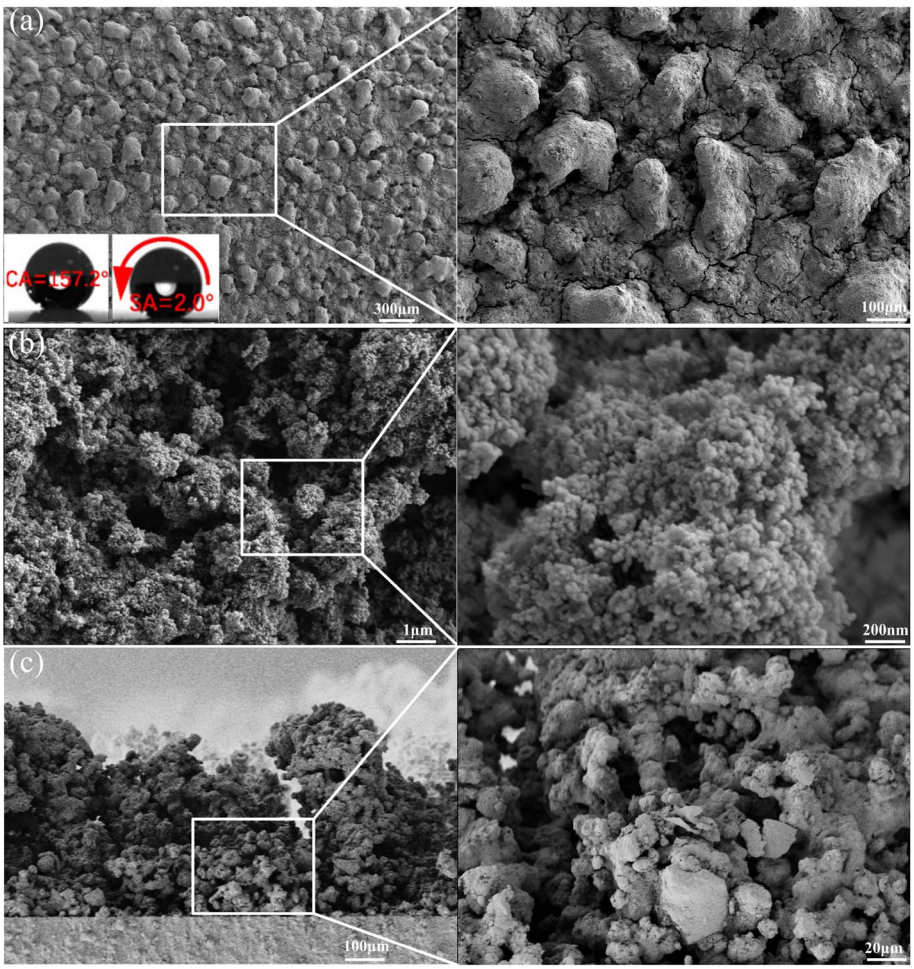

Fig. 2 Microstructural characterization of the superhydrophobic coating. (a) Surface SEM micrograph demonstrating the micro-nano hierarchical roughness; (b) discrete epoxy resin microspheres serving as the core durability-enhancing constituent; and (c) cross-sectional view revealing a gradient porous architecture extending throughout the coating thickness.

crucial for achieving and maintaining a stable Cassie–Baxter wetting state.

The microstructure of the epoxy-based superhydrophobic coating was systematically characterized using scanning electron microscopy (SEM). SEM micrographs (Fig. 2a) reveal that the silica nanoparticles spontaneously aggregate on the coating surface, forming irregular protrusions exhibiting micro-nano hierarchical morphology. Such micro-nano composite rough structures are recognized as essential morphological features for achieving superhydrophobic surfaces with low adhesion. Crucially, the hierarchical gaps formed between ridge-like micro-convex bodies play a pivotal role in the hydrophobic mechanism by stabilizing the entrapped air (or gas cushion) at the solid–liquid interface, which is consistent with the Cassie–Baxter wetting state.

The core of our coating design lies in the blending mechanism between the discrete epoxy micro-aggregates and the modified nanoparticles. The high-resolution SEM image presented in Fig. 2b shows that the SiO_2@PFDTES nanoparticles are not embedded but are firmly anchored on the surface of the epoxy spheres. Combined with the uniform F distribution from EDS (Fig. 1c), this visual evidence strongly supports a co-assembly mechanism during the spray deposition and solvent evaporation processes. Crucially, cross-sectional morphological analysis (Fig. 2c) confirms the formation of an internal, three-dimensionally interconnected, multi-level pore network within the coating.

The formation of this distinctive gradient porous architecture can be attributed to the deliberate induction of epoxy resin phase separation. The dropwise addition of a poor solvent (absolute ethanol) into the epoxy-butyl acetate solution destabilizes the polymer solution, leading to the formation of discrete, micron-sized epoxy resin aggregates *via* a nucleation and growth process. During the subsequent spray-coating and solvent evaporation, these rigid resin aggregates do not coalesce into a continuous film. Instead, they serve as primary building blocks, co-assembling with the SiO_2@PFDTES nanoparticles. The nanoparticles adsorb onto the surfaces of the resin aggregates, and together, they pack into a three-dimensionally interconnected network. The rapid solvent evaporation 'freezes' this co-assembled structure, creating a mechanically robust scaffold with hierarchical porosity. This inherent, gradient roughness throughout the coating's cross-section is the fundamental morphological feature that differentiates our coating from conventional ones and underlies its exceptional durability.

3.2 Analysis of the superhydrophobic properties

The coating surface demonstrates exceptional static superhydrophobicity, exhibiting a WCA as high as 157.2° ± 0.8° and a RA as low as 2.0° ± 0.2° (Fig. 3a). To further investigate the dynamic superhydrophobic properties, the bouncing behavior of 20 μL distilled water droplets was analyzed using a high-speed camera system. The droplets were released from a height of 10 mm onto the coating surface. As depicted in the time-series images (Fig. 3), upon initial contact (defined as t = 0 ms), the droplet undergoes compression and deformation, reaching its maximum spread at t = 41.6 ms. Complete rebound and detachment from the surface occur at t = 51.6 ms. The droplet attains its maximum rebound height at t = 96.6 ms and achieves a wetting equilibrium state after three distinct bounces. This remarkable dynamic response, characterized by a solid–liquid contact time of only 10 ms, originates from the synergistic effect of the micro-nano hierarchical roughness constructed by the silica nanoparticles and discrete resin microaggregates, coupled with the low surface energy imparted by the PFDTES modification. This combination effectively stabilizes the Cassie–Baxter wetting state, resulting in extremely low adhesion, evidenced by a contact angle hysteresis (CAH) of approximately 2.5°.

3.3 Mechanical and chemical stability tests

Mechanical and environmental durability represent critical parameters for the practical deployment of the superhydrophobic coatings. In this work, the coating's durability was

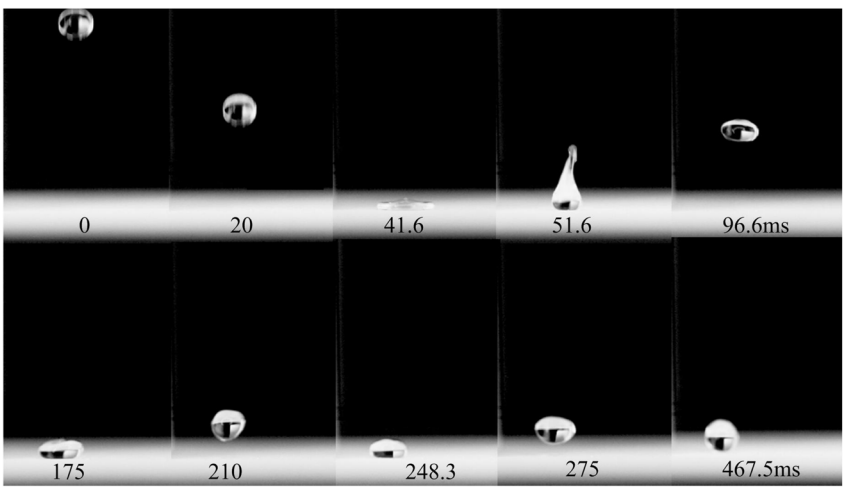

Fig. 3 Bouncing behavior of a 20 μL water droplet on the coated surface.

comprehensively assessed using a suite of tests, including linear abrasion against sandpaper, tape peeling, immersion in deionized water and chemical solutions, accelerated ultraviolet (UV) aging, and thermal cycling.

The mechanical durability of the superhydrophobic coating was evaluated through linear abrasion testing against sandpaper. The experimental results demonstrate that the coating maintained superhydrophobicity (WCA: 150.2° ± 1.5°; RA: 6.1° ± 0.5°) until reaching an abrasion distance of 16.4 m, beyond which the WCA decreased below 150° (Fig. 4a). Microstructural evolution analysis revealed the underlying failure mechanism: the pristine surface exhibited densely distributed micro-nano hierarchical roughness (Fig. 4b). Following 8 m of abrasion (Fig. 4c and d), the partial degradation of the surface topography occurred, though newly exposed regions retained substantial roughness. Ultimately, at a 20 m abrasion distance (Fig. 4e), complete structural collapse resulted in the morphological flattening and irreversible loss of air-cushion stabilization capability. Compared with that of the one-step sprayed superhydrophobic coatings documented in literature,[21–24] the critical abrasion distance in this study increased significantly to 16.4 m (Fig. 4f).

This remarkable enhancement in abrasion resistance is directly attributable to the 'structural regeneration' mechanism enabled by the gradient porous network. In conventional one-step sprayed coatings, abrasion removes the nanoparticle-rich surface layer, exposing a smooth, dense polymer underlayer that lacks the necessary roughness and low surface energy,

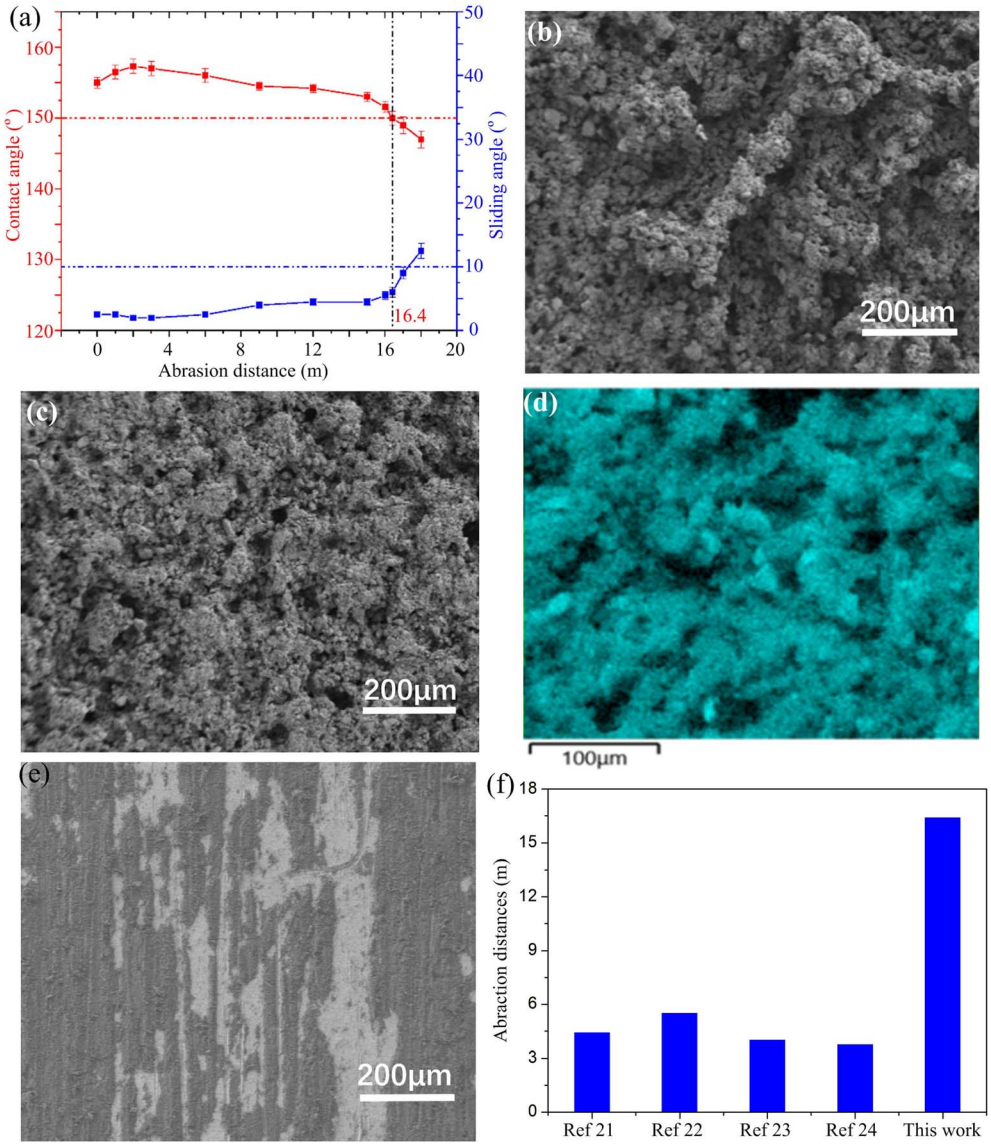

Fig. 4 Evaluation and comparative analysis of the wear resistance of the coated sample. (a) Evolution curve of the superhydrophobicity with wear distance; (b and c) SEM images depicting the surface morphology at wear distances of 0 m and 8 m; (d) elemental distribution maps of F-element; (e) SEM images depicting the surface morphology at a wear distance of 20 m; and (f) comparison of the wear resistance with those of existing studies. Data are presented as mean ± standard deviation ($n = 5$).

leading to immediate failure. In contrast, the structure of our coating is uniform in its roughness throughout its thickness. As the top layer is worn away (Fig. 4c), the newly exposed surface is not a smooth polymer matrix but is, in fact, a sub-surface layer of the same co-assembled structure, replete with epoxy aggregates and nanoparticles. The SEM image (Fig. 4c) and the corresponding EDS F-element map (Fig. 4d) show that the newly exposed surface retains a rough microstructure and a homogeneous distribution of fluorine. This provides direct physicochemical evidence that the removal of the top layer exposes a sub-surface with similar composition and morphology, effectively validating the proposed 'structural regeneration' mechanism inherent to our design. This ensures that the critical micro-nano topography and low surface energy characteristics are preserved upon abrasion, allowing the coating to maintain the Cassie–Baxter state until the material is substantially consumed (Fig. 4e).

To assess the interfacial bonding strength, tape peel testing was performed. A quantitative assessment (Fig. 5a) demonstrated the retention of superhydrophobicity through 37 peel cycles (WCA: 150.3° ± 1.2°; RA: 7.5° ± 0.8°), with subsequent degradation reducing the WCA below 150°. Microstructural evolution analysis *via* SEM revealed that the pristine surface maintained intact micro-nano composite topography (Fig. 5b); after 15 peel cycles (Fig. 5c and d), localized delamination occurred in discrete regions, though newly exposed interfaces preserved low-surface-energy characteristics. After 50 cycles (Fig. 5e), nanoparticle cluster detachment induced significant roughness reduction, consequently compromising the Cassie–Baxter stability and superhydrophobic functionality.

To gain a deep understanding of the failure mechanism and to validate the 'structural regeneration' concept under peeling stress, we characterized the coating surface after 15 peel cycles using SEM and EDS. The SEM image presented in Fig. 5c shows localized delamination in discrete regions, which is expected from a tape-peeling process. Critically, the newly exposed surfaces in these regions are not smooth but display a residual micro-nano roughness. The corresponding EDS elemental map for fluorine (Fig. 5d) confirms that this underlying surface remains rich in low-surface-energy components, with a homogeneous distribution of F elements comparable to that of the pristine coating. These observations provide compelling physicochemical evidence for the proposed mechanism: the coating does not fail through a simple adhesive loss at the substrate interface but through a cohesive failure within the coating's thickness. More importantly, because the coating's composition and structure are uniform throughout its bulk (as seen in the cross-section, Fig. 2c), the sub-surface exposed by peeling is inherently superhydrophobic. This self-similarity in both morphology and chemical composition from the top surface to the bottom is the key to the coating's remarkable peeling resistance, ensuring that its functionality is not compromised by localized mechanical damage.

Fig. 6a depicts the evolution of WCA and RA as functions of thermal cycling frequency. Each thermal cycle comprised sequential 20 min holds: first at −20 °C, followed by immediate transfer to 150 °C. Quantitative analysis revealed sustained superhydrophobicity through 12 cycles, with WCA maintained at 156.3° ± 1.1° and RA at 2.5° ± 0.4° – values are statistically indistinguishable from initial measurements. This thermal

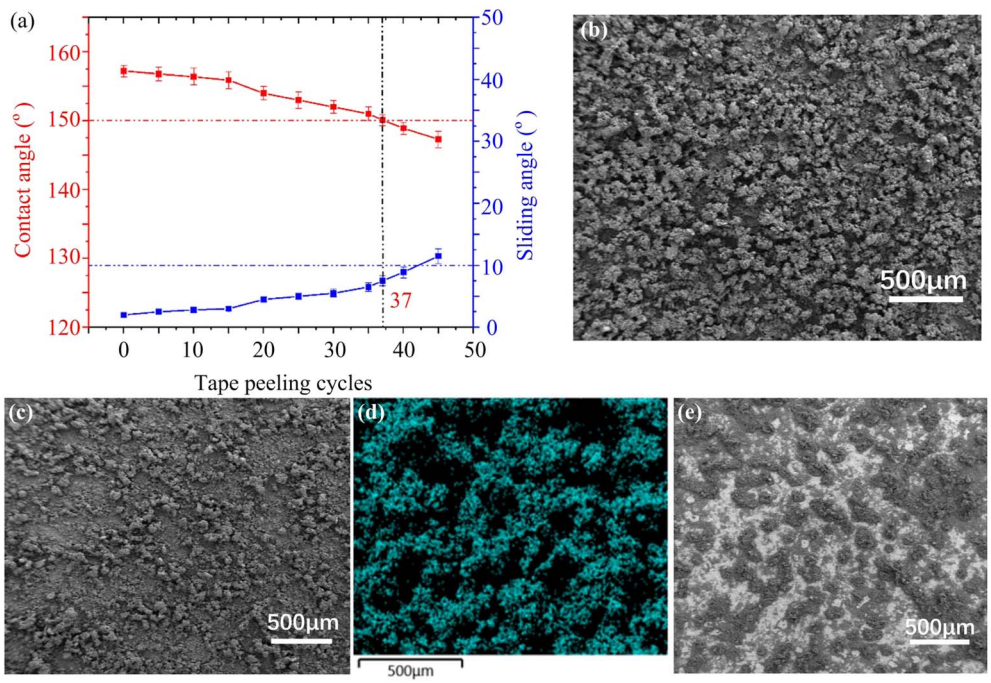

Fig. 5 Investigation of the peeling behavior of the coated sample. (a) Evolution curve of the superhydrophobicity with the peeling cycles; (b and c) SEM images showing the surface morphology after 0 and 15 peeling cycles; (d) elemental distribution maps of F-element; and (e) SEM images showing the surface morphology after 50 peeling cycles. Data are presented as mean ± standard deviation ($n = 5$).

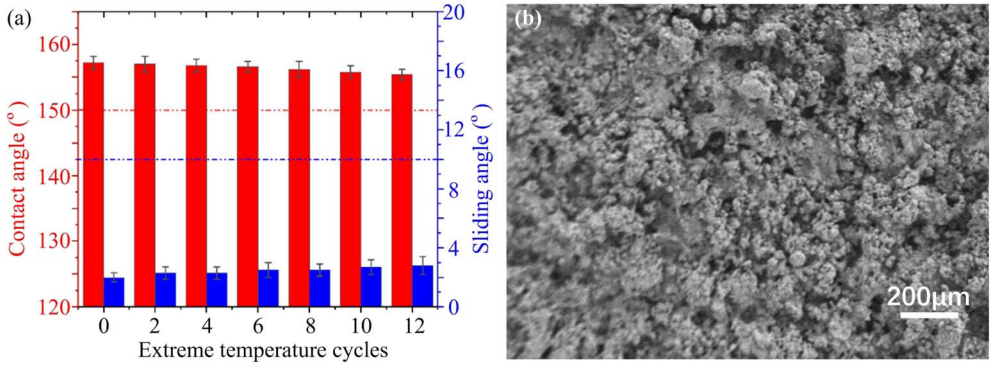

Fig. 6 Investigation of the coating tolerance to thermal cycling. (a) Evolution of the superhydrophobicity with the thermal cycling count; (b) post-cycling surface morphology characterized by SEM. Data are presented as mean ± standard deviation ($n = 5$).

invariance confirms the exceptional thermomechanical stability. Complementary SEM analysis (Fig. 6b) corroborates these findings, demonstrating preserved micro-nano hierarchical surface topography after thermal stressing with no observable cracking or structural degradation compared with the pristine coating.

To quantitatively evaluate long-term anti-wetting stability under immersion conditions, samples underwent complete submersion in deionized water for 336 h (14 days). Hydrophobic performance was monitored at 24 h intervals through WCA and RA measurements, with temporal evolution data presented in Fig. 7a. Results demonstrate exceptional stability retention: post-immersion WCA remained at 155.7° ± 1.2°, and RA stabilized at 4.2° ± 0.6°. This sustained superhydrophobicity confirms the micro-nano hierarchical architecture's superior capability to stabilize the entrapped air film at solid–liquid interfaces throughout prolonged aqueous exposure, which is consistent with robust Cassie–Baxter state maintenance.

Furthermore, chemical durability was evaluated using aggressive media, including HCl (pH = 2), NaOH (pH = 12), and 3.5 wt% NaCl solutions. Following a 240 h (10 days) immersion in either acidic or alkaline corrosive environments, the coatings maintained robust superhydrophobicity (Fig. 7b). Significantly, exposure to chloride-rich conditions (3.5 wt% NaCl, 240 h) revealed exceptional stability against ionic penetration, with negligible variation in hydrophobic performance. This corrosion resistance originates from the intrinsic chemical inertness of the fluorinated epoxy matrix and PFDTES-modified nanoparticles, complemented by the persistent air barrier stabilized at the solid–liquid interfaces through the Cassie–Baxter state maintenance.

To assess operational stability under simulated outdoor conditions, accelerated ultraviolet aging tests were conducted using a UV irradiator ($\lambda = 365$ nm, 5800 mW cm^{-2}). WCA and RA measurements were recorded at 60 min intervals during continuous irradiation. As quantified in Fig. 7c, the coating retained exceptional superhydrophobicity after 12 h of cumulative exposure (WCA: 156.7° ± 1.3°; RA: 2.5° ± 0.2°). This photostability demonstrates negligible UV-induced degradation, confirming suitability for extended outdoor applications. Collectively, these results establish the coating's robust performance across extreme service environments – including mechanical abrasion, chemical corrosion, and UV irradiation – attributable to the synergistic stability of fluorinated components and persistent cassie-state air entrapment.

Collectively, the outstanding performance across all durability tests—abrasion, peeling, chemical, UV, and thermal cycling—stems from a synergistic combination of two factors: (1) the robust and regenerable gradient microstructure provided by the discrete epoxy binder system, which ensures the physical preservation of the Cassie–Baxter state, and (2) the intrinsic chemical inertness and stable low surface energy

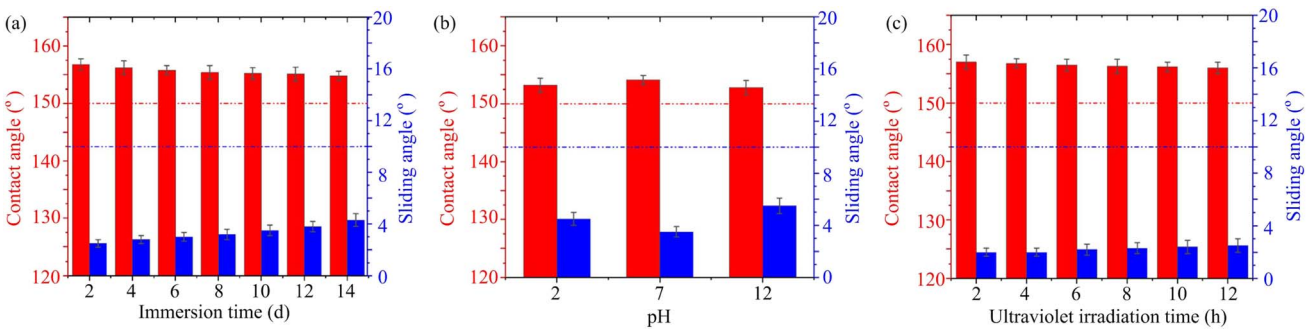

Fig. 7 Characterization of the environmental tolerance for the coated samples. (a) Liquid penetration resistance; (b) chemical corrosion resistance; and (c) UV-aging resistance. Data are presented as mean ± standard deviation ($n = 5$).

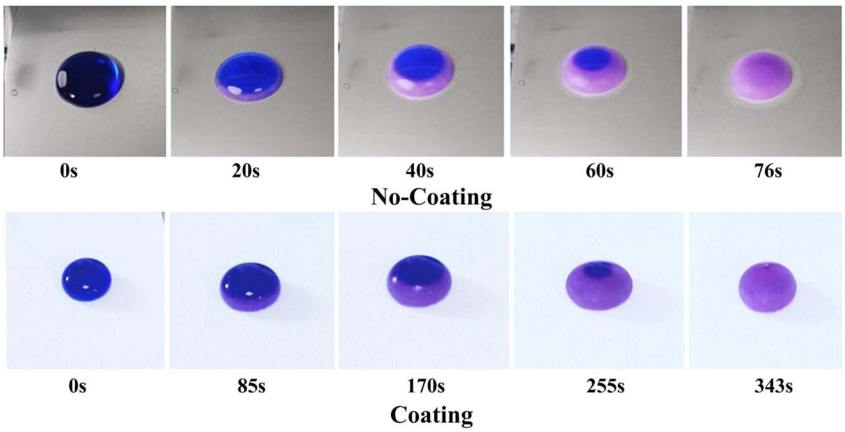

Fig. 8 Delayed icing effect of the coatings.

imparted by the fluorinated epoxy matrix and the PFDTES modification. The three-dimensional porous network not only facilitates mechanical durability but also stabilizes a persistent air barrier at the solid–liquid interface, which acts as a shield against corrosive media and water penetration.

3.4 Anti-icing performance

The ice delay performance of the coating was evaluated by recording the freezing time of the water droplets (500 μL) at −20 °C. As shown in Fig. 8, the water droplet on the bare substrate froze within 76 s. In stark contrast, the freezing time was significantly delayed to 343 s on our superhydrophobic coating. This remarkable delay is attributed to the stable air cushion trapped in the hierarchical micro-nano structure, which effectively reduces the solid–liquid contact area and acts as a thermal barrier, thereby retarding heat transfer and ice nucleation. The outstanding anti-icing performance confirms the practical utility of our coating. The discrete epoxy binder-derived gradient porous structure is not only crucial for mechanical durability but also fundamental for maintaining a stable non-wetting state against water and ice. This synergy between robust microstructure and superior icephobicity makes our coating a promising candidate for protecting outdoor equipment and infrastructures from icing hazards.

4. Conclusion and outlook

This study successfully engineered a superhydrophobic coating system employing discrete epoxy microaggregates as the binding matrix and fluorosilane-modified silica nanoparticles for constructing micro-nano hierarchical surface roughness. This design effectively addresses the critical durability-stability trade-off inherent in conventional one-step sprayed superhydrophobic coatings. Experimental validation demonstrates the following. (i) Abrasion-triggered subsurface pore exposure enables continuous roughness regeneration, significantly extending the critical wear distance; (ii) synergistic air-cushion stabilization *via* cassie-state maintenance and inherent chemical inertness confers exceptional tolerance to extreme environments—maintaining stable superhydrophobicity after exposure to concentrated corrosive media (>240 h), thermal shock cycling (12 cycles, −20 °C ↔ 150 °C), and intensive UV irradiation (12 h, 5800 mW cm^{-2}). This work establishes a robust material platform for durable superhydrophobic applications in demanding operational contexts, including corrosion/ice mitigation on aircraft engine blades, marine equipment protection, arctic infrastructure anti-icing, and photovoltaic panel soiling mitigation.

Despite the significant enhancement in the mechanical durability achieved by our discrete epoxy binder strategy, this study has specific limitations that point toward future research opportunities. First, the current formulation is optimized for a specific set of parameters (*e.g.*, epoxy type, nanoparticle loading, and solvent ratio). A more systematic investigation into the relationship between the phase separation kinetics, the size of the epoxy micro-aggregates, and the resulting coating performance could yield a predictive model for further optimization. Second, while the coating demonstrates excellent passive anti-icing performance by delaying ice formation, its active de-icing capabilities (*e.g.*, photothermal or electrothermal de-icing) were not explored. Incorporating functional nanomaterials to endow the coating with such on-demand de-icing properties is a highly attractive future direction. Lastly, the long-term environmental stability beyond our tested accelerated aging conditions, particularly under real-world, multi-factor outdoor exposure for several years, requires further validation to fully assess the commercial viability and service life of the coating. Addressing these aspects in future work will not only deepen the fundamental understanding of such durable superhydrophobic systems but also substantially broaden their application scope in more demanding and intelligent scenarios.

Author contributions

Writing – original draft, X. L.; supervision, X. L. and L. W.; project administration, X. L.; funding acquisition, X. L.; validation, X. Z. and X. L.; investigation, X. L.; formal analysis, X. Z.; writing – review and editing, X. L., X. L., X. Z. and L. W. All

authors have read and agreed to the published version of the manuscript.

Conflicts of interest

There are no conflicts to declare.

Data availability

All data that support the findings of this study are included within this article.

Acknowledgements

The authors acknowledge the support from the National Science Foundation of China (Grant No. 22203038); and the Doctoral Research start-up fund: XBQ202027. We appreciate Beijing High-Throughput Technology Co., Ltd. for their valuable assistance in data analysis.

References

1 W. Barthlott and C. Neinhuis, Purity of the sacred lotus, or escape from contamination in biological surfaces, *Planta*, 1997, **202**, 1–8.
2 M. Ma and R. M. Hill, Superhydrophobic surface, *Curr. Opin. Colloid Interface Sci.*, 2006, **11**(4), 193–202.
3 P. Roach, N. J. Shirtcliffe and M. I. Newton, Progress in superhydrophobic surface development, *Soft Matter*, 2008, **4**, 224–240.
4 X.-M. Li, D. Reinhoudt and M. Crego-Calama, What do we need for a superhydrophobic surface? A review on the recent progress in the preparation of superhydrophobic surfaces, *Chem. Soc. Rev.*, 2007, **36**, 1350–1368.
5 A. B. D. Cassie and S. Baxter, Wettability of porous surfaces, *Trans. Faraday Soc.*, 1944, **40**, 546–551.
6 C. Li, N. Li, X. Zhang, Z. Dong, H. Chen and L. Jiang, Uni-Directional Transportation on Peristome-Mimetic Surfaces for Completely Wetting Liquids, *Angew. Chem., Int. Ed.*, 2016, **55**(48), 14988–14992.
7 D. Wang, Q. Sun, M. J. Hokkanen, C. Zhang, F.-Y. Lin, Q. Liu, S.-P. Zhu, T. Zhou, Q. Chang, B. He, Q. Zhou, L. Chen, Z. Wang, R. H. A. Ras and X. Deng, Design of robust superhydrophobic surfaces, *Nature*, 2020, **582**, 55–59.
8 Z. Liu, Y. Si, C. Yu, L. Jiang and Z. Dong, Bioinspired superwetting oil–water separation strategy: toward the era of openness, *Chem. Soc. Rev.*, 2024, **53**, 10012–10043.
9 H. Gao, Y. Liu, G. Wang, S. Li, Z. Han and L. Ren, A multifunctional graphene composite coating with switchable wettability, *Chem. Eng. J.*, 2021, **415**, 128862.
10 H. Wang, Z. Zhang, Z. Wang, J. Zhao, Y. Liang, X. Li and L. Ren, Improved dynamic stability of superomniphobic surfaces and droplet transport on slippery surfaces by dual-scale re-entrant structures, *Chem. Eng. J.*, 2020, **394**, 124871.
11 W. Xu, Y. Jin, W. Li, Y. Song, S. Gao, B. Zhang, L. Wang, M. Cui, X. Yan and Z. Wang, Triboelectric wetting for continuous droplet transport, *Sci. Adv.*, 2022, **8**(51), 2085.
12 S. Feng, P. Zhu, H. Zheng, H. Zhan, C. Chen, J. Li, L. Wang, X. Yao, Y. Liu and Z. Wang, Three-dimensional capillary ratchet-induced liquid directional steering, *Science*, 2021, **373**(6561), 1344–1348.
13 H. Guo, Y. Wang, H. Zhang and K. An, Recent advances and strategies in mechanical stability of superhydrophobic surfaces, *Prog. Org. Coat.*, 2024, **194**, 108595.
14 M. Z. Khan, J. Militky, M. Petru, B. Tomkova, A. Ali, E. Toren and S. Perveen, Recent advances in superhydrophobic surfaces for practical applications: A review, *Eur. Polym. J.*, 2022, **178**, 111481.
15 Y. He, L. Wang, T. Wu, Z. Wu, Y. Chen and K. Yin, Facile fabrication of hierarchical textures for substrate-independent and durable superhydrophobic surfaces, *Nanoscale*, 2022, **14**, 9392.
16 C. Zhang, K. Pei, J. Zhao, Y. Zhou, S. Zhang, X. Han and Z. Guo, Hierarchical dandelion-like superhydrophobic surfaces with excellent stability and photothermal performance for efficient anti-/deicing, *Chem. Eng. J.*, 2025, **510**, 161582.
17 Z. Huang, S. Zhu, M. Zhu, Y. Tian and L. Ma, A durable superhydrophobic surface with bud-particle structure prepared by one-step spray method, *Appl. Surf. Sci.*, 2025, **679**, 161255.
18 P. Yu, Z. Yu, K. Liao, S. Xia, K. Li and J. Chen, Preparation of superhydrophobic coatings by saturated fatty acid modification using a one-step spraying method, *Appl. Surf. Sci.*, 2025, **690**, 162612.
19 Z. Liu, N. Xu, X. Yu, C. Yang and H. Chu, Preparation of superhydrophobic coatings with excellent mechanical and chemical stability by one-step spraying method with selected fluorine-free modifiers, *Appl. Surf. Sci.*, 2024, **642**, 158635.
20 X. Lei, L. Hao, G. Jian, *et al.*, Large-scale fabrication of decoupling coatings with promising robustness and superhydrophobicity for antifouling, drag reduction, and organic photodegradation, *Friction*, 2023, **11**, 716–736.
21 J. Su, F. Su, H. Yu, *et al.*, Synthesis of superhydrophobic FAS-EP/PTFE coating with excellent drag reduction performance and mechanical robustness, *Appl. Surf. Sci.*, 2023, **634**, 157644.
22 Y. Zhao, M. Huo, J. Huo, *et al.*, Preparation of silica-epoxy superhydrophobic coating with mechanical stability and multifunctional performance via one-step approach, *Colloids Surf. A*, 2022, **653**, 129957.
23 Z. Wang, X. Liu, J. Ji, *et al.*, Underwater Drag Reduction and Buoyancy Enhancement on Biomimetic Antiabrasive Superhydrophobic Coatings, *ACS Appl. Mater. Interfaces*, 2021, **13**(40), 48270–48280.
24 H. Pakzad, M. Liravi, A. Moosavi, *et al.*, Fabrication of durable superhydrophobic surfaces using PDMS and beeswax for drag reduction of internal turbulent flow, *Appl. Surf. Sci.*, 2020, **513**, 145754.

25 C. Zhang, K. Pei, T. Sheng, *et al.*, Metal oxides engineering: toward sustainable superhydrophobic surfaces, *Adv. Funct. Mater.*, 2025, e12239.
26 Y. Cao, C. Wang, F. Tie, *et al.*, Superhydrophobic alkoxysilane/T-ZnO/SiO2 nanocomposite coatings enhance mechanical properties of porous building substrates: An experimental and multi-physics simulation study, *Constr. Build. Mater.*, 2025, **467**, 140412.
27 H. Chen, Y. Cao, C. Wang, *et al.*, Superhydrophobic surfaces for the sustainable maintenance of building materials and stone-built heritage: The challenges, opportunities and perspectives, *Adv. Colloid Interface Sci.*, 2025, **335**, 103343.
28 J. Wei, B. Li, N. Tian, *et al.*, Scalable robust superamphiphobic coatings enabled by self-similar structure, protective micro-skeleton, and adhesive for practical anti-icing of high-voltage transmission tower, *Adv. Funct. Mater.*, 2022, **32**, 2206014.
29 J. Wei, J. Zhang, X. Cao, *et al.*, Durable superhydrophobic coatings for prevention of rain attenuation of 5G/weather radomes, *Nat. Commun.*, 2023, **14**, 2862.